Research Square

Preprints are preliminary reports that have not undergone peer review.
They should not be considered conclusive, used to inform clinical practice,
or referenced by the media as validated information.

Distinct periodic behaviour of long- and short-period atmospheric gravity waves and their wind filtering in the MLT region

Kiran Kiran
Physical Research Laboratory
Ravindra Pratap Singh
ravindra@prl.res.in

PRL: Physical Research Laboratory https://orcid.org/0000-0001-5636-4899

Research Article

Keywords: PRL Airglow InfraRed Spectrograph (PAIRS), OH(3-1) Nightglow emission and Rotational temperature, MLT dynamics, Short and long period atmospheric gravity waves (AGW), Wind filtering of upward propagating AGWs, wave period for upward propagation

Posted Date: June 24th, 2026

DOI: https://doi.org/10.21203/rs.3.rs-9898953/v1

License: This work is licensed under a Creative Commons Attribution 4.0 International License.
Read Full License

Distinct periodic behaviour of long- and short-period atmospheric gravity waves and their wind filtering in the MLT region

Kiran[a,b], Ravindra P. Singh[a,*]

[a]Space and Atmospheric Sciences Division, Physical Research Laboratory, Navrangpura, Ahmedabad, 380009, India

[b] Indian Institute of Technology, Gandhinagar, 382355, India

[*] Corresponding author

E-mail addresses: vishukiran@prl.res.in (Kiran); ravindra@prl.res.in (Ravindra P. Singh)

Keywords: PRL Airglow InfraRed Spectrograph (PAIRS); OH(3-1) Nightglow emission and Rotational temperature; MLT dynamics; Short and long period atmospheric gravity waves (AGW), Wind filtering of upward propagating AGWs; wave period for upward propagation

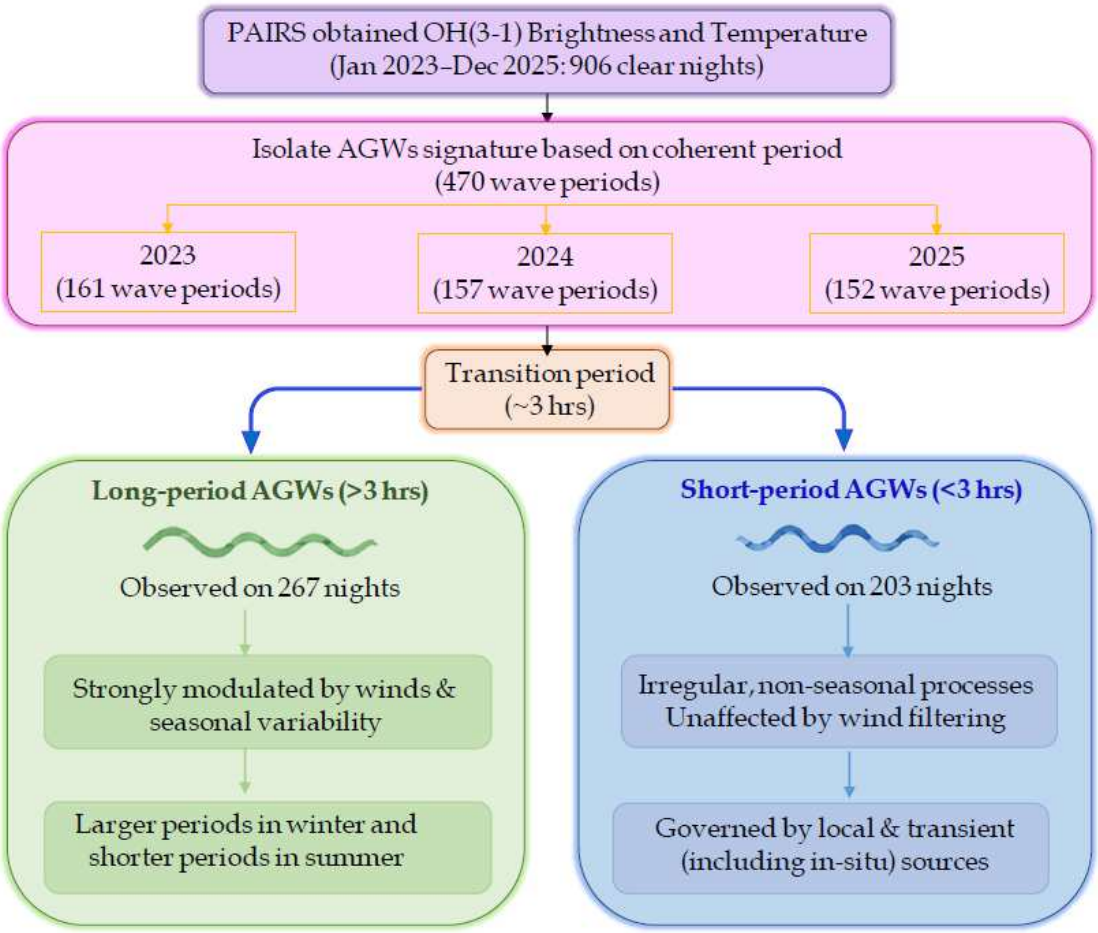
Highlights

- Wave periodicities are analysed using OH(3–1) nightglow brightness and corresponding rotational temperatures.
- Atmospheric gravity waves with periodicities more than 3 hrs exhibit clear seasonal variability.
- The seasonal variation in wave periods shows a strong positive correlation with the background horizontal wind in the MLT region.

Abstract

This study investigates the seasonal variability of Atmospheric Gravity wave (AGW) activity in the Mesosphere and Lower Thermosphere (MLT) region, with a particular focus on its seasonal dependence on wave period. Using three years (January 2023–December 2025) of continuous observation of OH(3–1) nightglow brightness and rotational temperature obtained from the ground-based PRL Airglow Infrared Spectrograph (PAIRS), AGW periods are systematically analyzed. Out of 1096 observational nights, 906 (~83%) have ≥5 hrs of continuous data. From the nocturnal variations of brightness and temperatures, tidal components are removed, and a 3-hr moving average is applied to isolate AGW signatures. The Lomb–Scargle periodogram is employed to identify significant periodicities, and only coherent wave periods observed in both brightness and temperature are considered for statistical analysis. The results reveal a clear transition period of ~3 hrs, which delineates two distinct wave regimes; short- and long-period AGWs, observed on a total of 203 and 267 nights, respectively. Waves with periods greater than 3 hrs are controlled by large-scale wind filtering and seasonal variability, with longer periods observed during winter and shorther periods during summer. In contrast, waves with periods less than 3 hrs show irregular, non-seasonal processes. Analysis with HWM14-derived winds indicates that long-period wave variability is strongly modulated by background winds, particularly the meridional component. A high correlation (R = 0.89) between long-period waves and total horizontal wind highlights the role of wind filtering in which favourable wind conditions enable slow-moving waves to propagate upward. Conversely, short-period waves remain largely unaffected by wind filtering and are instead governed by local and transient sources, potentially including in situ generation within the MLT region.

Graphical Abstract



1. Introduction

Atmospheric gravity waves (AGWs) are crucial for vertical coupling of the atmosphere by transporting energy and momentum from the lower atmosphere to the mesosphere and lower thermosphere (MLT) region (Garcia and Solomon, 1985). These waves significantly influence the thermal structure, residual circulation, and overall MLT dynamics. However, the ability of these waves to propagate vertically is not solely determined by their intrinsic properties but is strongly controlled by the background atmospheric conditions, especially the horizontal wind field. Winds significantly influence the propagation of AGWs by altering their intrinsic frequency, changing their vertical wavelength, creating critical levels for dissipation, and acting as a filter for wave directionality (Fritts and Alexander, 2003).

Upward propagation of waves is governed by their phase speed relative to the background winds; unfavourable conditions lead to critical level interactions and subsequent dissipation before reaching higher altitudes (Dunkerton, 1982; Taylor et al., 1993). In contrast, very short-period waves are often not subject to such propagation constraints, as they are believed to be generated locally through rapid instabilities and wind-wave interactions within the atmosphere (Taylor & Hapgood, 1990; Hecht et al., 1997). Consequently, the observed wave spectrum is not a direct representation of the source distribution but is significantly modified by the intervening wind field (Cao and Liu, 2022; Ejiri et al., 2003). It is shown that the AGW's activity in MLT region exhibits strong period dependence, with shorter-period waves (<60 min) showing minimal seasonal variability, while longer-period waves (>240 min) display a dominant annual cycle with a winter maximum (Sedlak et al., 2020). A clear distinction exists between long-period and short-period waves in the MLT regon in terms of seasonal variability. Ground-based airglow observations are extensively used to investigate AGWs, particularly those with long vertical wavelengths and short horizontal wavelengths, as well as their seasonal behaviour (e.g., Taylor, 1997; Tang et al., 2002; Shiokawa et al., 2009; Singh & Pallamraju,

2016, 2017). However, despite the important role of wind filtering, there is still a lack of a clear quantitative understanding of the transition between wind-controlled and source-controlled AGW regimes.

Measurements of OH(3–1) emission brightness and the corresponding rotational temperature, derived from the same vibrational band, are widely used to investigate the characteristics of vertically propagating waves in the MLT region (Krassovsky et al., 1977; Tarasick and Hines, 1990; Wüst et al., 2023; Singh et al., 2023). When an AGW propagates vertically, it induces fluctuations in both the brightness and temperature. The observed phase difference between brightness and rotational temperature oscillations primarily arises due to their effective altitude separation within the OH emission layer. Satellite observations and modeling studies have shown that the peak of brightness perturbations occurs at an average altitude of ~3.5 km below the peak of the Volume Emission Rate (VER), whereas the rotational temperature perturbations are more closely aligned with the VER peak itself (Lowe et al., 1996; Swenson and Gardner, 1998; Liu and Swenson, 2003; Kiran and Singh, 2025a). As a result, brightness and temperature effectively sample the same wave at two nearby but distinct altitudes and can be used to estimate wave characteristics using Krassovsky ratio method, such as periodicity, vertical wavelength, and phase speed of AGWs in the MLT region (Singh et al., 2023; Kiran and Singh, 2025a) and their seasonal variation at low latitude (Singh and Pallamraju, 2017).

In this study, we primarily focus on identifying a transition period that distinguishes different regimes of wave behaviour, specifically separating waves that exhibit seasonal variability from those that do not. This distinction determines which waves are predominantly controlled by background horizontal winds and which are governed mainly by local, in-situ source mechanisms. For this purpose, three years (January 2023 to December 2025) of OH(3–1) nightglow brightness and corresponding rotational temperature observations have been utilized, obtained from the PRL Airglow InfraRed Spectrograph (PAIRS) over Ahmedabad

(23°N, 72.6°E). Wave periods are systematically estimated following the methodology described in Section 2.2, and their statistical distribution across all observational nights is presented in the Results and Discussion section. Since wave propagation is strongly influenced by background horizontal winds (Taylor et al., 1993, 1997; Hecht et al., 2001), winds derived from the Horizontal Wind Model (HWM) are incorporated to examine the seasonal variability of the observed waves. Furthermore, the study quantifies the threshold period up to which waves exhibit clear seasonal dependence on horizontal winds, with detailed analysis and interpretation provided in the results and discussion section.

2. Data used and Analysis method

2.1. Data set

A. PAIRS

PAIRS is a grating-based spectrograph designed to observe hydroxyl (OH) nightglow emissions over Ahmedabad (23°N, 72.6°E) in the short-wave infrared wavelength range of 1.5–1.6 μm. It provides simultaneous measurements of OH(3–1) airglow brightness and the corresponding rotational temperature. The rotational temperature is derived using three specific rotational emission lines, $P_1(2)$, $P_1(3)$, and $P_1(4)$, of the OH(3–1) Meinel band (e.g., Singh et al., 2023). These temperatures effectively capture wave activities and various atmospheric oscillations present in the MLT region (Kiran and Singh, 2025a, 2025b). Out of a total of 1,096 nights of PAIRS observations during January 2023 to December 2025 we considered only those nights having 5 hrs of continuous observation for each night which account for 906 nights

(83%). The variation in nighttime observational duration (in hrs) used for the derivation of wave periods is shown in Figure 1(a).

From Figure 1, it is evident that during the winter season (October to February), the longest observation durations, ranging between 11 to 13 hrs, are most frequently recorded. In contrast, the shortest observation durations occur during the monsoon months. Between March and September, the observations predominantly fall within the 9 to 11 hrs range. Reduced data availability during the monsoon season is primarily due to rainfall and cloud cover, which introduce artefacts into the observations. These affected data points are removed during preprocessing, leading to a decrease in usable nighttime observations during this period.

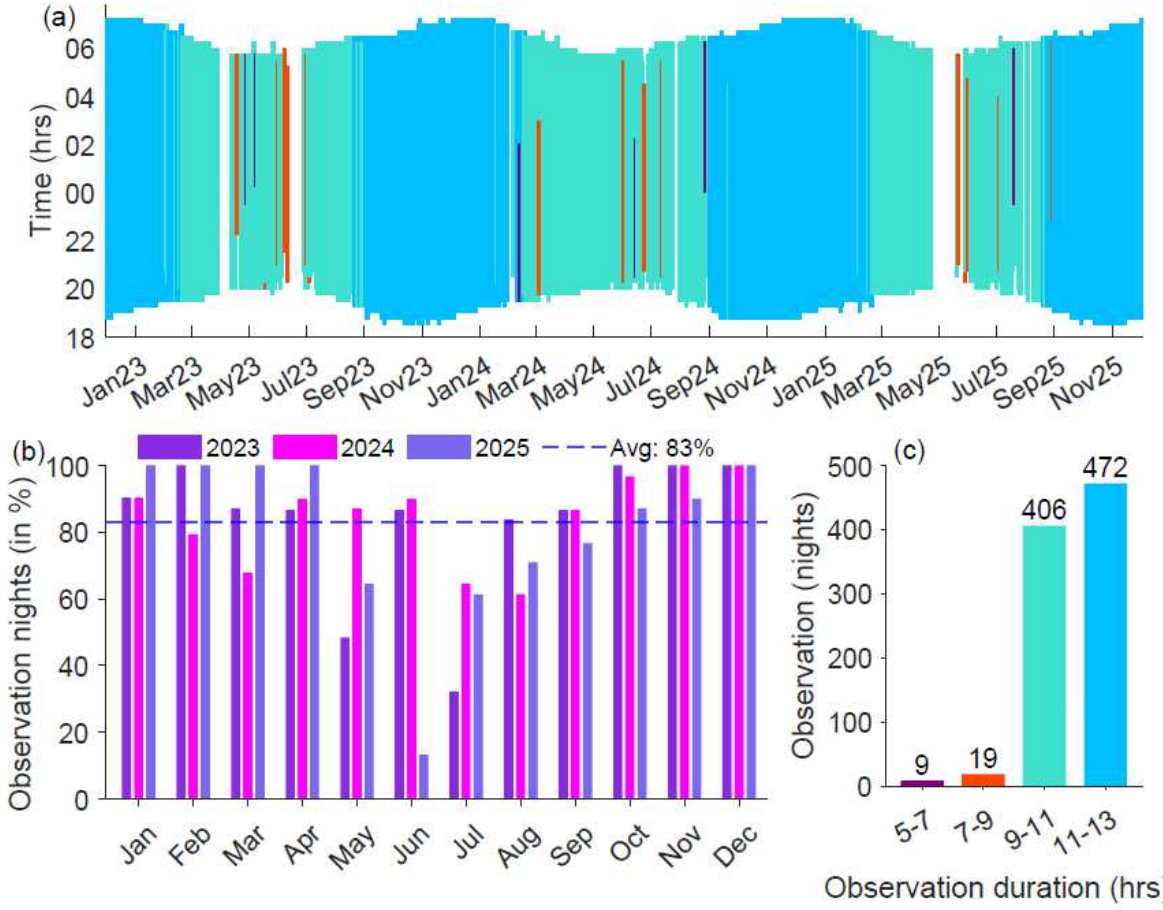


Figure 1: (a) Total time (in hrs) of continuous observation obtained from PAIRS over Ahmedabad during the period from January 2023 to December 2025. (b) Monthly percentage of available observational nights for the years 2023, 2024, and 2025, represented as colour-coded bars. The dotted line indicates the overall average availability of observational nights

(83%). (c) Total number of observational nights corresponding to the observation duration, with the values indicated above each bar. The bar colours are consistent with those used in Figure 1(a).

The monthly distribution of observations, shown in Figure 1(b), presents the percentage of total observations for each month across all three years. The Figure clearly indicates that a substantial number of nights are available for analysis in almost every month, demonstrating consistent data coverage throughout the year. The number of observational nights for every 2 hrs observation duration starting from 5 hrs are shown in Figure 1(c) highlighting the availability of observations with longer time durations. The distribution of nighttime observation durations shows that the majority of nights (52%; 472 nights) have durations of 11-13 hrs. This is followed by 45% (406 nights) of nights with durations ranging from 9 to 11 hrs with only 2% (19 nights) of nights falling within the 7 to 9-hrs range and just 1% (9 nights) within the 5 to 7-hrs range. Figure 1 shows that a significant portion of the dataset consists of extended nighttime measurements, which are sufficient for conducting detailed AGW studies presented in this work.

B. HWM

HWM is a globally recognized empirical framework designed to simulate and predict the horizontal neutral wind patterns across a vast vertical range, extending from the Earth's surface into the upper thermosphere (Drob et al., 2015). By synthesizing decades of satellite, rocket, and ground-based observations, the model generates comprehensive zonal (east-west) and meridional (north-south) wind vector fields. These outputs are calculated as a function of latitude, longitude, altitude, day of the year (DOY) and the specific time of day. In this study, HWM14-derived nighttime zonal and meridional wind components have been utilized over Ahmedabad (23°N, 72.6°E) at an altitude of 87 km, covering the period from January 2023 to December 2025. These model winds are used to examine the seasonal variability of the

158 background flow and to identify the transition wave period for AGWs that are subjected to
159 wind filtering effects.

160 **2.2 Analysis method**

161 **A. Removal of tidal component from nocturnal variation**

162 Low-latitude regions are primarily dominated by tidal activity, with the diurnal tide generally
163 exhibiting larger amplitudes than the semidiurnal and terdiurnal components (e.g., Deepa et al.,
164 2006; Smith, 2012). Consequently, to accurately investigate AGW characteristics, it is
165 necessary to first remove these tidal contributions from the nightly data. In this study, the tidal
166 effects are removed by performing sinusoidal curve fitting for both the diurnal and semidiurnal
167 components using Equation (1).

168 $$y = D_1 sin\left(\frac{2\pi}{24} * t + \phi_1\right) + D_2 sin\left(\frac{2\pi}{12} * t + \phi_2\right) + C \quad (1)$$

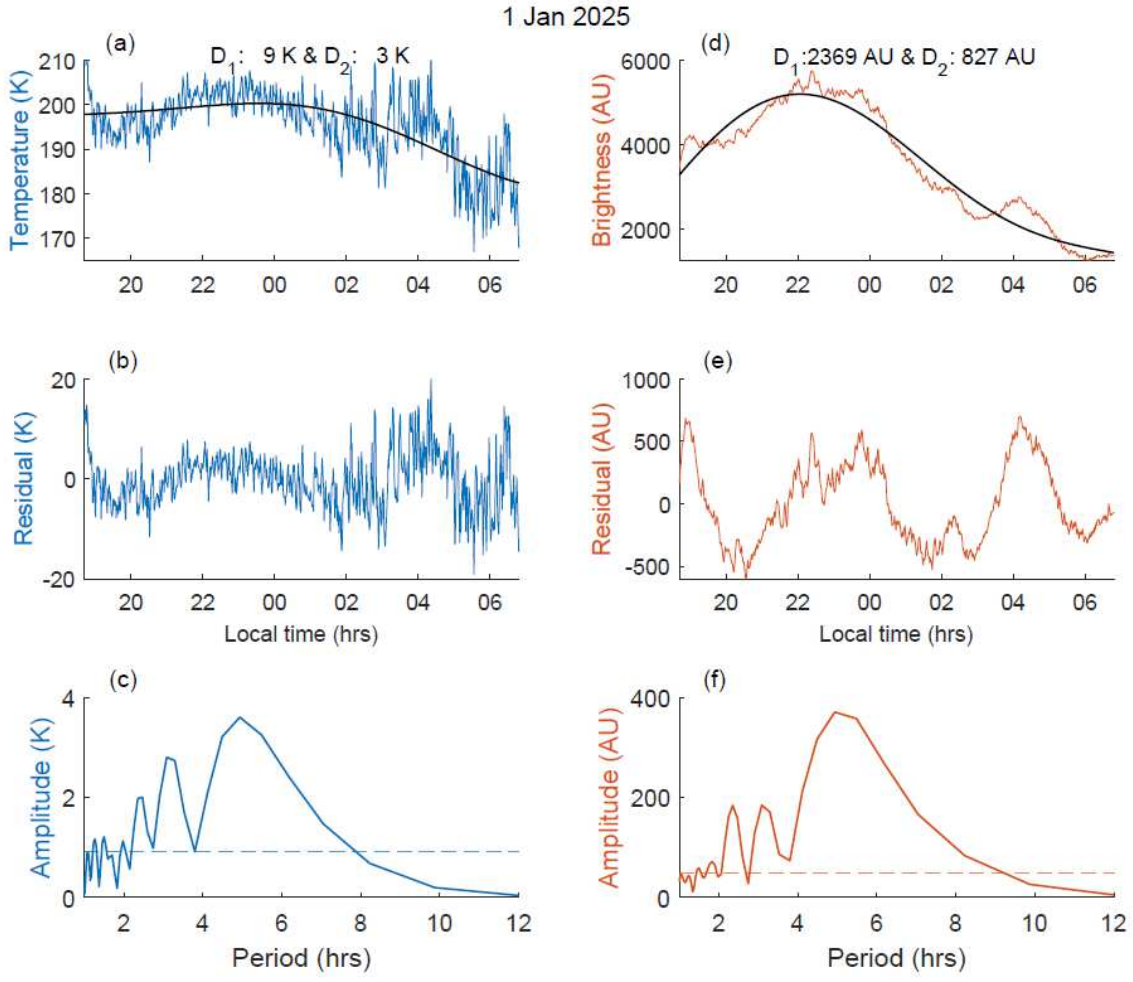


Figure 2: (a) Nocturnal variation in temperature observed on the night of 1 January 2025. The black curve represents the tidal variation obtained by fitting Equation (1). The amplitudes of the diurnal and semidiurnal tidal components are indicated at the top. (b) Residual temperature variations obtained after subtracting the fitted tidal component from the observed temperature. (c) Lomb–Scargle spectral analysis of the residual temperature, revealing multiple statistically significant periodicities. (d), (e), and (f) are similar to Figures (a), (b), and (c), respectively, but correspond to brightness variations for the same night. The horizontal dashed lines indicate the 95% confidence levels.

Where D_1 is diurnal amplitude, D_2 is semidiurnal amplitude, t is the time step, and ϕ_1 and ϕ_2 are the phases of the diurnal and semidiurnal tidal components, respectively.

Figure 2 presents the nocturnal variation of the OH(3–1) rotational temperature and brightness on 1 January 2025, displayed in the left and right panels, respectively. The observed temperature and brightness are represented by blue and orange curves, while the fitted tidal components are overlaid as black curves. From the fitting, D_1 and D_2 are estimated to be 9 K and 3 K for temperature, and 2369 AU and 827 AU for brightness, respectively. Figures 2(b) and 2(e) show the residuals obtained after subtracting the fitted tidal components from the nocturnal variations of temperature and brightness, respectively. These residuals are further analyzed to identify the periodicities of AGWs present during the night.

To determine the dominant periodicities, spectral analysis is performed using the Lomb–Scargle periodogram (Lomb, 1976; Scargle, 1982). This method is particularly suitable for the present dataset, as the observations contain gaps arising from artifacts such as moonlight, cloud cover, and stray light contamination (Hocke and Kämpfer, 2009; Hocke, 1998). The results of the spectral analysis of the residuals are presented in Figures 2(c) and 2(f) for temperature and brightness, respectively, with consistent colour representation used for both parameters.

B. Derivation of AGW periodicities

Simultaneous nocturnal variation in OH(3-1) brightness and rotation temperature are used to derive the AGW characteristics. The vertical AGW characteristics from the OH emission layer are obtained using Krassovsky ratio method which is interpreted to be due to a small altitude difference between peak perturbations in brightness and rotational temperature occurring at distinct altitudes within the OH layer (Krassovsky et al., 1977; Swenson and Gardner, 1998; Kiran and Singh, 2025a). This altitude separation within the layer is interpreted as the primary cause of the observed phase difference between the coherent periods detected in brightness and temperature, a phenomenon that facilitates the calculation of vertical wave parameters such as wavelength and phase speed (Reisin and Scheer, 1996).

In order to investigate the seasonal variation of AGWs' activity having short and long periodicities a transition period of 3 hrs is selected as a reference threshold for further analysis. To isolate the relevant wave components, a 3-hr moving average is applied to the tidal-removed temperature (skyblue) and brightness (orange) residuals and are shown in blue and red curves in Figures 3(a) and 3(b), respectively. It is important to note that the time series has been truncated by 1.5 hrs at both the beginning and the end when applying the 3-hr moving average. This is done to avoid edge effects (or moving average bias), which arise because the averaging window is incomplete at the boundaries. By removing these portions, the moving average is computed only where a full 3-hr window is available, ensuring more reliable and unbiased determination of the periods from the obtained residuals. The maximum cross correlation between 3-hr moving average temperature and brightness is found to be 0.96, indicating similar variations in both the parameters. This peak cross correlation occurs at a lag of 26 data points, which corresponds to shifting brightness by 0.5 hrs earlier compared to the temperature, demonstrating vertical propagation of the wave through OH emission layer.

Subsequently, a Lomb–Scargle periodogram spectral analysis is performed on 3-hr moving average temperature and brightness residuals, and the results are displayed together in Figure

3(c) using the corresponding colour scheme. The analysis reveals presence of coherent periodicity of 5.3 hrs in both temperature and brightness. This periodicity is marked by a black vertical dotted line in Figure 3(c). Further a sine curve corresponding to the identified 5.3 hrs period is fitted using equation 2 and overlaid on the 3 hrs moving averaged temperature and brightness.

$$y = \mathrm{A}\sin\left[\left(\frac{2\pi}{\tau}\right) * \mathrm{t} + \phi\right] + \mathrm{c} \qquad (2)$$

Where A is the amplitude, τ is the period, t is the time step, and ϕ is the phase of the wave. The fitted curves are shown in Figures 3(a) and 3(b) in purple and magenta, for temperature and brightness, respectively. The corresponding amplitude (A) and phase (ϕ) values are indicated at the top of Figures 3(a) and 3(b). For temperature, the amplitude and phase are 1.9 K and 0.8 radians, respectively, while for brightness, they are 196 AU and 0.2 radians, respectively.

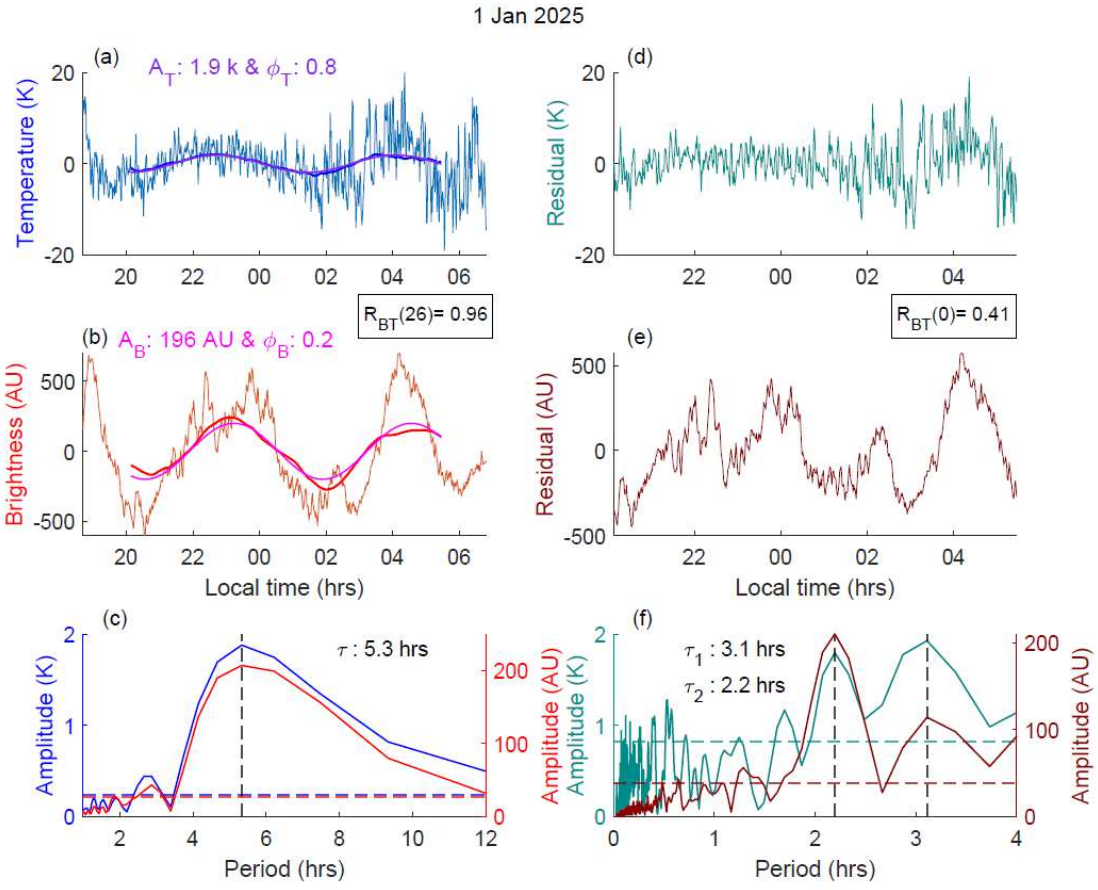


Figure 3: (a) 3-hr moving average is applied to the temperature residuals after removing the tidal components (sky blue) represented as blue curve. (b)The same procedure is applied to the brightness residuals after removing the tidal components (orange) represented as red curve. The maximum cross correlation between 3-hr moving average brightness and temperature is found to be 0.96, as indicated in the text box. (c) Spectral analyses of 3-hr moving average temperature and brightness residuals, highlighting a coherent period of 5.3 hrs, marked by vertical dotted lines. The purple and magenta curves in (a) and (b) represent the sine curve fitting of a 5.3 hrs period obtained using equation (2). The amplitudes and phase values derived from this fitting are displayed at the top of Figures 3(a) and 3(b). Figures (d) and (e) show the residuals obtained after subtracting the fitted sine curve from the 3-hrs moving average temperature and brightness time series, respectively. (f) presents the Lomb–Scargle spectral analysis of the residuals, revealing the presence of coherent periods at 3.1 hrs and 2.2 hrs. The horizontal dashed lines represent the 95% confidence levels.

We have used Krassovsky's ratio method to calculate the AGW characteristics of the upward propagating waves through the OH emission layer (Krassovsky et al., 1977; Tarasick and Hines, 1990; Reisin and Scheer, 1996; Kiran and Singh, 2025a). The negative phase difference between brightness and temperature ($\phi_B - \phi_T = -0.6$ radians) for the wave having coherent period of 5.3 hrs indicate the upward propagation of the wave. The Krassovsky's ratio method is employed to estimate the vertical wavelength using the relation, $\lambda_z = \frac{2\pi\gamma \mathrm{H}}{(\gamma-1)|\eta|\sin\phi}$ and the corresponding vertical phase speed $\left(C_z = \frac{\lambda_z}{\tau}\right)$. Here, $\eta, \left(= \frac{\mathrm{A_B}/\bar{\mathrm{B}}}{\mathrm{A_T}/\bar{\mathrm{T}}}\right)$ represents the Krassovsky's parameter, A_B and A_T are the amplitudes of brightness and temperature, and $\bar{B}$ and $\bar{T}$ are their respective mean values. The parameter γ = 1.4 is the ratio of specific heats at constant pressure and volume. H is the atmospheric scale height, H = KT/mg, where T is taken as the PAIRS measured nightly mean temperature. Using the observed data, the calculated values of η and H

255 are ~5.8 and ~5.9 km, respectively. The derived λ_z and C_z for the ~5.3 hrs period wave
256 observed on this night are estimated to be ~44.3 km and ~8.4 km/hr, respectively.

257 To identify periodicities less than 3-hrs, residuals are obtained by subtracting 3-hrs moving
258 average (shown as the blue and red curves in Figure 3(a) and 3(b) for temperature and
259 brightness, respectively) from the tidal-removed variations (depicted as sky-blue and orange
260 curves in Figures 3(a) and 3(b) for temperature and brightness, respectively). The resulting
261 residuals are presented in Figure 3(d) and 3(e), where temperature and brightness variations
262 are shown in seagreen and maroon colours, respectively. The peak of the cross correlation
263 coefficients between these two residuals is found to be 0.41 at a lag of 0, which means that
264 both variables vary simultaneously without any time delay between them, as highlighted in the
265 textbox shown in the Figure 3(e). The corresponding spectral analysis of these residuals is
266 illustrated in Figure 3(f), using the same colour scheme. The spectral results reveal two
267 coherent periodicities at ~3.1 hrs and ~2.2 hrs, which are clearly identified as dominant peaks
268 and marked by vertical dotted black lines in the Figure 3(f). It should be noted here that merely
269 observing the coherent periods in brightness and temperature does not ascertain vertical
270 propagation of the AGW. Hence, we have used Krassovsky's ratio method, which states that a
271 negative value of $\phi_B - \phi_T$, indicate the vertical propagation of the wave through OH emission
272 layer.

273 The analysis method is applied to all 906 nights to identify wave periods based on the coherence
274 between temperature and brightness variations. Only those nights that exhibit coherent
275 periodicity in both parameters and a negative value of $\phi_B - \phi_T$ are considered as valid wave
276 signatures. Using this approach, wave periods range from as short as 0.3 hrs (approximately 18
277 minutes) to as long as 6.9 hrs. The lower limit exceeds the Brunt–Väisälä period, which ranges
278 from approximately 4.6 to 5.2 minutes for the OH* airglow layer, with some seasonal and
279 geographical variability (Wüst et al., 2020). The upper limit of 6.9 hours corresponds to nearly

half of the maximum nighttime duration (~13 hours), thereby ensuring the reliable detection of longer-period waves within the available observational window. For further analysis, the identified waves are categorised into two groups based on their periods. The first category includes short-period waves, which does not show vertical propagation and periodicities ranging from 18 minutes to 3 hrs, while the second category consists of longer-period waves, which show vertical propagation with periods between 3 and 6.9 hrs. This classification enables a systematic investigation of the seasonal variability of the periodicities of the short and long period waves as well as the influence of wind filtering on their propagation characteristics.

3. Results and discussions

a. Distribution of wave occurrence across different period ranges

Figure 4 presents the occurrence of nights exhibiting wave activity across different period ranges (0–1 to 6–7 hrs) for the years 2023, 2024, and 2025. Each year is separated by dashed vertical lines for a comparative analysis of wave occurrence patterns over time. A total of 161 nights in 2023, 157 nights in 2024, and 152 nights in 2025 exhibited coherent periodicities in both brightness and temperature. From Figure 4, it is evident that wave occurrences are not uniformly distributed across all period ranges.

In 2023, the highest number of occurrences is observed in the 5–6 hr period range, followed by 4–5 hrs, indicating a dominance of longer-period waves during that year. Periods shorter than 3 hrs are moderately represented, while the shortest (0–1 hr) and longest (6–7 hrs) periods show very few occurrences. A similar pattern is observed in 2024, where the 5–6 hr period again records the highest occurrence. However, compared to 2023, there is a slight redistribution, with relatively higher occurrences in the 1–2 hr range, suggesting a broader spread of wave activity across different periods. In 2025, the dominance of the 5–6 hr period becomes even more pronounced, showing the highest occurrence among all three years,

followed by the 1–2 hr range. The 3–4 hr and 6–7 hr periods consistently exhibit lower occurrences across all years.

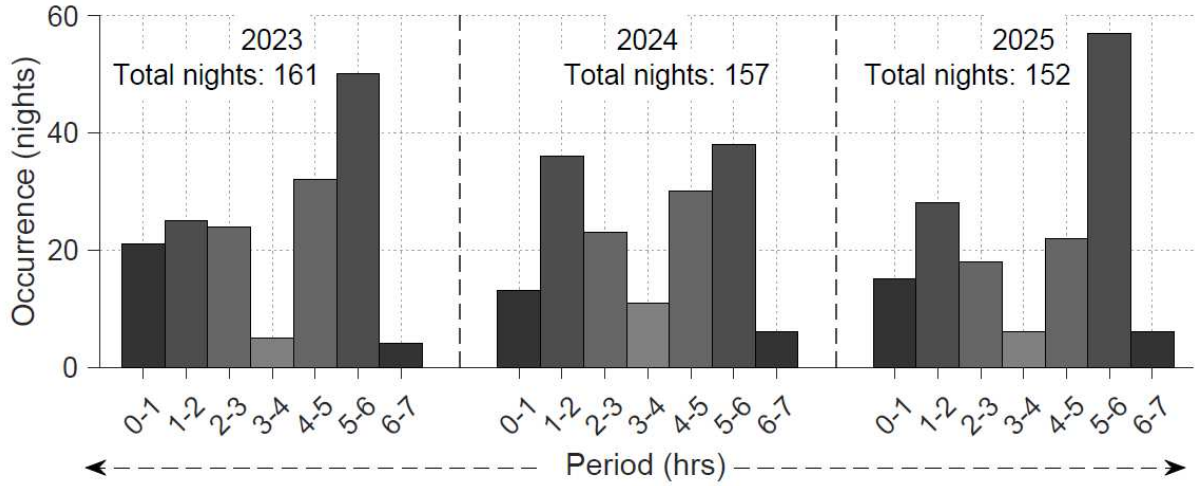


Figure 4: Occurrence of nights exhibiting coherent periods in both brightness and temperature during the years 2023, 2024, and 2025, shown separately with the total such nights for each year.

Overall, the results indicate that wave activity is most frequent in the mid- to long-period range, particularly between 4–6 hrs, with consistent contributions from shorter periods (1–3 hrs). A three-year averaged analysis reveals that waves with periods of 5–6 hrs occur on ~31% of the total nights showing coherent periods, making them the most dominant component of the wave spectrum. In comparison, shorter-period waves in the 1–2 hr range are observed on ~19% of the nights. This suggests favourable conditions for the generation or detection of waves within these ranges. For further investigation waves are categorized into two groups based on their periods: short-period waves (periods less than 3 hrs) and long-period waves (periods greater than 3 hrs). This classification allows for a more detailed comparison of their occurrence and behaviour, as these two categories are associated with different generation mechanisms and atmospheric conditions.

b. Monthly distribution of wave occurrence by period range

Figure 5 presents the monthly variation in the occurrence of nights (in percentage) exhibiting wave activity observed over a three-year period from 2023 to 2025, separated into two categories: (a) waves with periods less than 3 hrs and (b) waves with periods greater than 3 hrs. Over the three-year study period, a total of 203 nights exhibited the presence of short-period waves (< 3 hrs), whereas 267 nights showed clear evidence of long-period waves (with > 3 hrs). Figure 5(a) shows the moderate variability in the occurrence of short-period waves throughout the year. These short-period waves are distributed intermittently, without any seasonal peak. In contrast, Figure 5(b), which represents long-period waves, exhibits a clearer seasonal pattern. The occurrence is relatively high during the winter months (January–February), decreases during April-September, and then increases again toward the end of the year, reaching a peak in December. This indicates that long-period waves are more prominent during winter conditions.

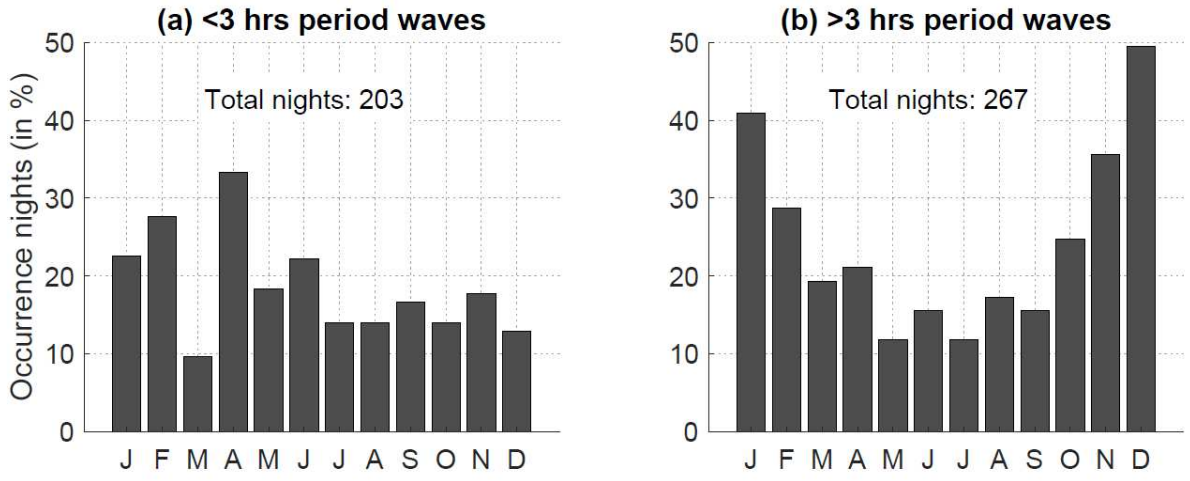


Figure 5: Monthly occurrence of nights (in percentage) observed over a three-year period from 2023 to 2025 is presented. (a) illustrates the occurrence of nights during which AGWs with periods shorter than 3 hrs are detected, whereas (b) shows the occurrence of nights associated with AGWs having periods longer than 3 hrs. The total number of nights on which such waves are observed is indicated within each figure.

Comparing both, the Figure 5 suggests a seasonal dependence of wave activity, with long-period waves dominating and showing enhanced occurrence during winter months, while short-period waves remain more uniformly distributed throughout the year.

c. Spectral analysis of wave periods

The nightly variation of the wave periods over a three-year span are illustrated for both long-period and short-period waves in Figure 6(a) and 6(b), respectively. The vertical error shows error in the derived periodicities using Lomb-Scargle method calculated using following formula $\delta f = \frac{1.1\sigma}{A\,T_{total}\sqrt{N}}$. Where σ represents the standard deviation of the frequencies associated with the subtracted variation, T_{total} is the total observation time, A is the amplitude of the variation, and N is the number of measurements (Bretthorst, 1988). The error in frequency δf is used to calculate the error in the corresponding periodicity. The long-period waves are observed for 91 days in 2023, 85 days in 2024, and 91 days in 2025. Whereas short-period waves are observed for 70 days in 2023, 72 days in 2024, and 61 days in 2025. A consistent colour scheme has been maintained in subsequent analyses for each year.

The Lomb–Scargle spectral analysis for these waves is presented in Figures 6(c) and 6(d). The results clearly demonstrate the periodic behaviour of long-period waves, with a prominent peak corresponding to the annual oscillation at 365 days, indicated by a black vertical dotted line in

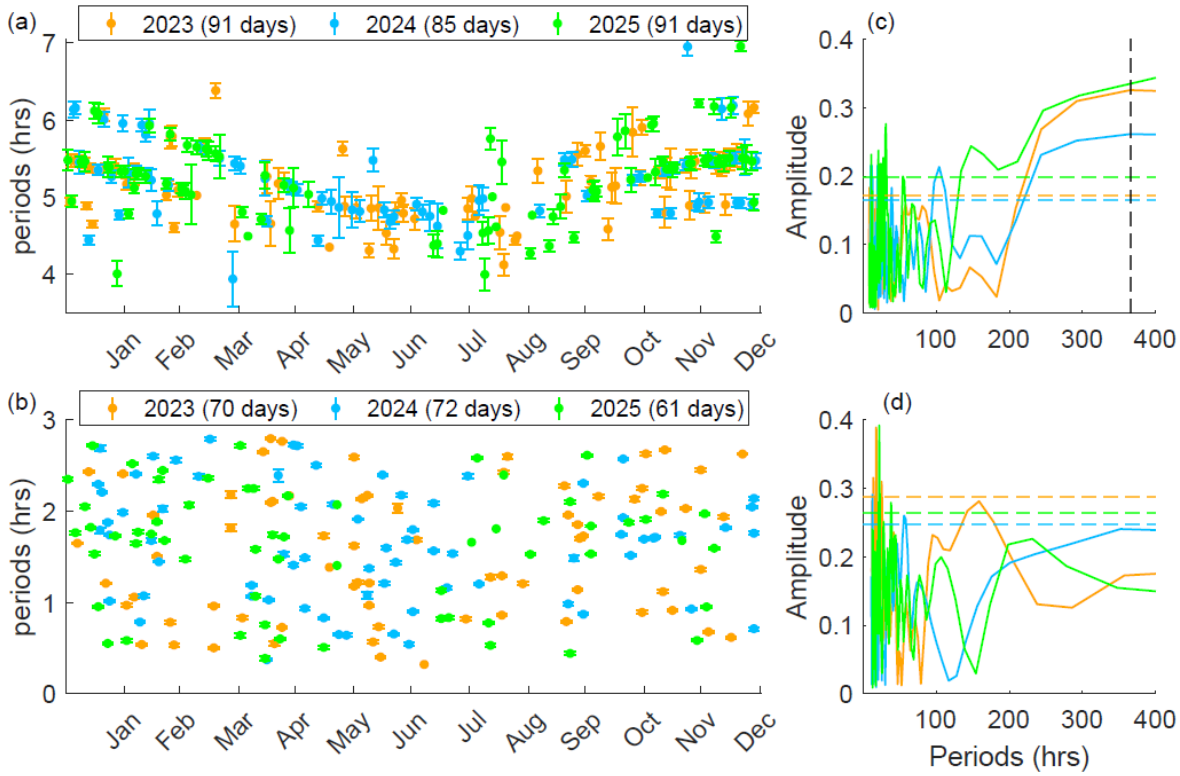


Figure 6: Nightly variation of the wave periods for three consecutive years are shown using different colours, as indicated in the legend, with the total number of observation days for each year provided alongside. (a) presents wave periods greater than 3 hrs, while (b) shows wave periods less than 3 hrs, distributed across different months. (c) and (d) display the corresponding spectral analyses of the wave periods for each year, using the same colour scheme. The horizontal dashed lines indicate the 95% confidence levels for the spectral peaks. The vertical black dashed line marks a common periodicity of 365 days, which is consistently observed and statistically significant across all three years.

Figure 6(c) for each year. The presence of this dominant annual oscillation throughout the year indicates that long-period wave activity is strongly modulated by seasonal atmospheric conditions, most likely through mechanisms such as background wind filtering. In contrast, the short-period waves exhibit a more random distribution, with no significant peaks observed in their spectral analysis, suggesting the absence of a dominant periodic pattern. This suggests that their occurrence is governed primarily by localized and transient processes rather than by large-scale background wave filtering of the vertical propagating AGWs.

d. Seasonal behaviour of long-period waves

To investigate the periodic behaviour of long-period waves, we utilized horizontal wind components derived from the HWM14 model. Since wind filtering acts as a selective barrier for AGWs propagating into the MLT region, the impact differs significantly based on the wave's phase speed and wavelength (Taylor et al., 1993; Kiran and Singh, 2025a).

The HWM14 model is used to calculate the nightly mean zonal (U_x) and meridional (U_y) wind components over Ahmedabad calculated at an altitude of 87 km averaged between 18 hrs to 6 hrs local time. The impact of background winds on long-period waves are analysed in Figure 7, which illustrates the relationship between wave periods and the U_y (Figure 7(a)) and U_x (Figure 7(b)) wind components across three-year (January 2023 to December 2025). The nightly variation of the long-time period wave is shown in Figures 7(a) and (b) with the same colour-coding scheme used in Figure 6 to distinguish periods of the consecutive years. The sinusoidal fit, represented by the dark cyan curve highlight a dominant annual periodicity of 365 days that persists across all three years of observation. The Lomb–Scargle spectral analysis reveal the presence of a coherent annual oscillations between the wave periods (dark cyan) and the wind components; U_y (blue) and U_x (red), as illustrated in the spectral distributions presented in Figures 7(b) and 7(d). A quantitative assessment indicates that variations in wave periods exhibit a stronger statistical coherence with the U_y (correlation coefficient R=0.78) than with U_x (R=0.68). These relatively high correlation values suggest that both wind components play a role in modulating wave propagation through mechanisms such as Doppler shifting and critical level filtering (Fritts and Alexander, 2003). However, despite the generally larger magnitude of annual oscillation in U_x (≈21 m/s) approximately 2.7 times that of U_y (≈8m/s), U_y appears to be the dominant factor governing the annual modulation of long-period AGWs in the MLT region over Ahmedabad.

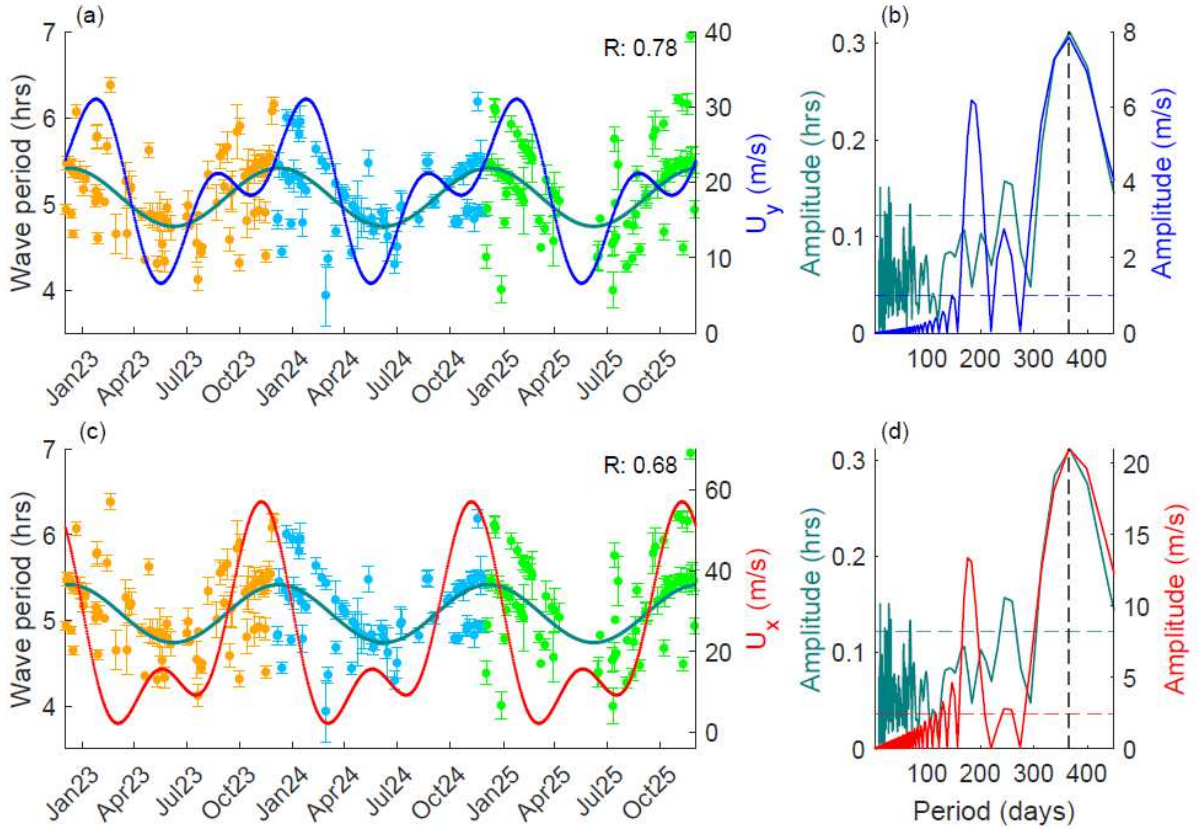


Figure 7: Nocturnal variation of the periodicities of the long period waves (left axis) are presented together with the nighttime MLT wind components (right axis) across all three years (2023 to 2025). In (a), the wave periods are shown along with the meridional wind component (blue). The dark cyan curve represents a sinusoidal fit corresponding to an annual (365-day) cycle, obtained from Lomb–Scargle spectral analysis of both the wave periods and the meridional wind, as illustrated in (b). The correlation coefficient (R) between the annual variation of the wave periods and the meridional wind component is indicated in the top-right corner of the Figure. (c) and (d) are similar to Figures (a) and (b), respectively, but correspond to the zonal wind component (red).

Long-period waves (>3 hrs) are characterized by relatively slow phase speeds, making them dynamically fragile. Due to their low propagation speeds, even moderate background winds can approach or match their phase speed, leading to enhanced wave–mean flow interactions (Fritts and Alexander, 2003). As a result, these waves are more susceptible to critical level

filtering and dissipation. Even a small variations in U_x or U_y can readily shift the intrinsic phase speed toward zero, causing the waves to encounter critical levels and subsequently attenuate or disappear from observations. In contrast, short-period waves (< 3 hrs) possess comparatively higher phase speeds, which allows them to propagate more robustly through the background flow. Their higher speeds make them less sensitive to moderate fluctuations in U_x and U_y, reducing the likelihood of critical level interactions.

e. Horizontal wind influence on wave periods

Given the contrasting dynamical behaviours of long- and short-period waves, both categories are analysed with the resultant horizontal wind (U_h), defined as $\left(U_h = \sqrt{\left(U_x^2 + U_y^2\right)}\right)$, as presented in Figures 8(a) and 8(b). The Lomb–Scargle spectral analysis of the wave periods and U_h is shown in Figures 8(b) and 8(d), respectively, where long-period waves and short-period waves are represented in dark cyan and U_h as black. The spectral analysis clearly reveals a pronounced annual cycle in both the long-period waves and U_h, as indicated by the prominent peak marked by the black dotted vertical line at a period of 365 days in Figure 8(b). In contrast, the analysis of shorter-period waves does not reveal any significant periodicity, implying that these periods are likely generated in-situ and dominated by irregular processes rather than a well-defined cycle. Furthermore, the high correlation coefficient of 0.89 between the long-period waves and U_h suggests that these two parameters are closely linked in their temporal variability. This suggests that changes in the background wind field play a dominant role in modulating the observed wave periods.

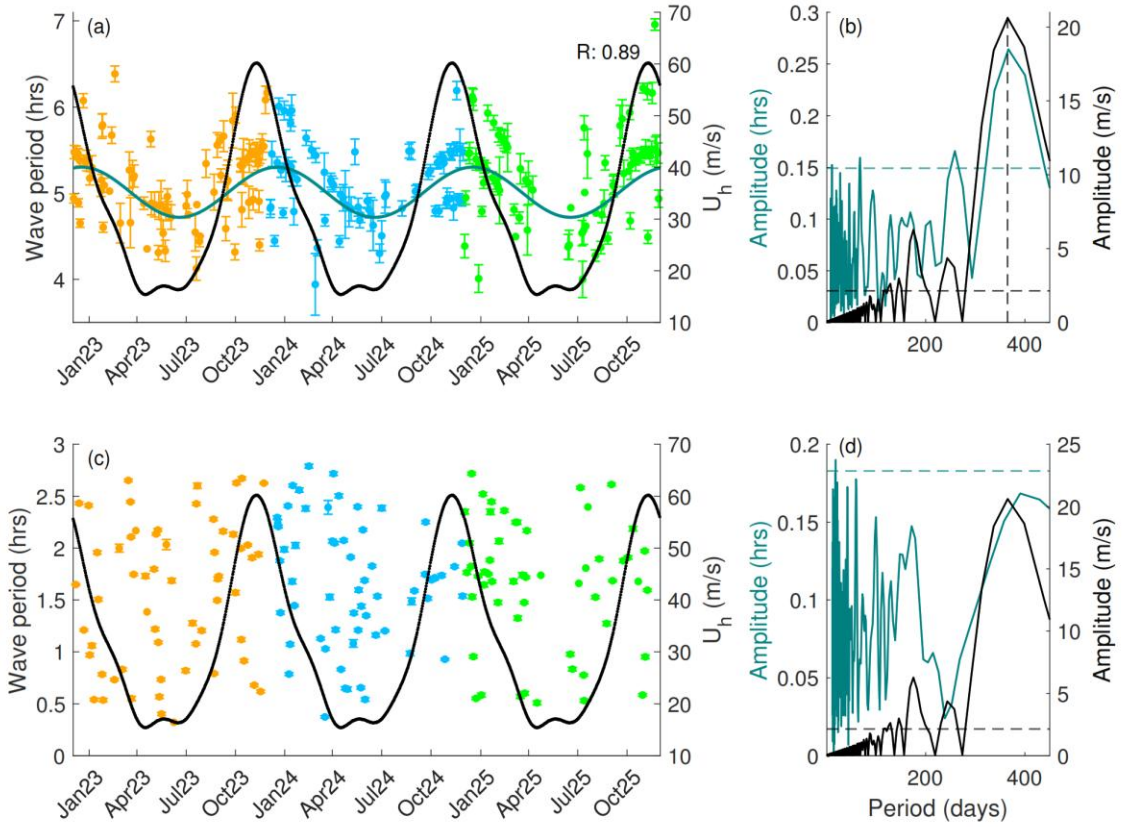


Figure 8: (a) showing the all the wave periods greater than 3 hrs (left axis) across all three year (2023 to 2025) together with the nighttime MLT horizontal wind (black, right axis). The dark cyan curve represents a sinusoidal fit corresponding to the dominant annual periodicity (365-day) in the wave periods derived from Lomb–Scargle spectral analysis, as illustrated in (b) for both the wave periods *and the horizontal wind* in their respective colours. *(c) displays wave periods less than 3 hrs for all three years, shown in their respective colours, along wit*h the horizontal wind (black). *(d) shows the corresponding spectral analysis, indicating the absence of any significant periodicity in the shorter-period wave variations.*

AGWs propagate upward only if their intrinsic phase speed, defined relative to the background wind, remains finite. Thus, upward propagation is permitted when $(c_h - U_h) \neq 0$, ensuring that the wave is not absorbed by the mean flow. The wave propagates vertically against the prevailing wind direction, and for long-period slow moving waves $(c_h \ll U_h)$ the intrinsic

441 phase speed is dominated by the background wind, making their propagation highly sensitive
442 to variations in the U_h. When U_h increases, the term $(c_h - U_h)^2$ for long-period waves also
443 becomes larger in the dispersion relation of AGWs, which leads to an increase in their vertical
444 wavelength (Hines, 1960; Fritts and Alexander, 2003). A larger vertical wavelength
445 corresponds to reduced vertical gradients in wave perturbations, which can delay the onset of
446 dynamical and convective instabilities, thereby allowing wave to be more stable, less prone to
447 breaking, and therefore more likely to propagate to higher altitudes and be observed more
448 frequently. Consequently, under favorable wind conditions, slow-moving waves with relatively
449 longer periods are shielded from reaching critical levels, allowing them to survive and
450 propagate into the upper atmosphere. This selective filtering mechanism causes the population
451 of long-period waves to vary systematically, leading to an observed in-phase relationship
452 between long period wave activity and U_h (Taylor et al., 1993; Hecht et al., 2001). This wind
453 filtering mechanism modulates the wave activity seasonally with enhanced occurrence during
454 winter months and reduced activity during summer months, consistent with the strong
455 correlation (R=0.89) shown in Figure 8(a).

456 In contrast, shorter period waves (< 3 hrs period) typically have much larger c_h ($\gg U_h$),
457 resulting in intrinsic phase speeds that are weakly influenced by background wind variations.
458 As a result, their vertical propagation is less sensitive to seasonal wind filtering, and they do
459 not exhibit a clear correlation with U_h, as seen in Figure 8(c). Instead, these waves are primarily
460 controlled by intermittent and localized source mechanisms, including deep convection,
461 localized instabilities, and wave breaking processes. In many cases, they may also be generated
462 in situ within the MLT region through wave-mean flow interaction, rather than propagating
463 upward from lower atmospheric layers. This distinction explain why their presence appears
464 irregular and uncorrelated with U_h, in contrast to long-period waves, which are strongly
465 modulated by wind filtering.

4. Summary

This study examines the seasonal variability of AGWs' activity in the MLT region, with particular emphasis on how this variability depends on wave period. The analysis specifically distinguishes between wave periods that exhibit a clear seasonal dependence and those that do not, enabling a more focused investigation of their physical origins: whether they are generated locally within the MLT region (in situ) or originate in the lower atmosphere and propagate upward. For this purpose, a continuous three-year observation (January 2023 to December 2025) of OH(3–1) nightglow brightness and rotational temperature measurements, obtained from the ground-based PAIRS instrument are utilized to derive AGW periodicities. Out of a total of 1096 nights, about 83% (906 nights) meet the criterion of having at least 5 hrs of continuous observations, with an average nightly observation duration of approximately 11 hrs. Notably, about 97% of these nights have observation lengths ranging between 9 and 13 hrs, providing a robust dataset for statistical analysis of AGW activity in MLT region. To ensure that the extracted signals predominantly represent AGW activity, the dominant tidal components, associated with large-scale regular atmospheric variations are first removed from the nightly observations. Subsequently, a 3-hr moving average is applied to the residual data, which helps suppress short-term fluctuations and enhances the identification of underlying AGWs signatures. This processing approach enables a more reliable characterization of AGW variability and its dependence on wave period across different seasons.

The Lomb–Scargle periodogram is employed as the primary spectral analysis tool, as it is well suited for identifying statistically significant periodicities in unevenly sampled atmospheric data. Only those wave periods that show coherent periodicities in both brightness and temperature are considered for further analysis. The vertical propagation of waves is confirmed by the downward phase progression, i.e. by a negative phase difference between brightness and temperature variations derived from sine curve fitting. Furthermore, by applying the

Krassovsky's ratio method, a representative wave with a period of ~5.3 hrs is identified on 1st January 2025, having λ_z of ~44.3 km and c_z of ~8.4 km/hr.

All coherent wave periods are systematically identified for both the 3-hr moving averaged data and the corresponding residuals for each night, ensuring a comprehensive capture of AGW activity across different temporal scales. Finally, a detailed statistical analysis of the wave periods over the three-year dataset is carried out, leading to key findings on the seasonal and non-seasonal behaviour of AGWs in the MLT region. The key findings of this study are summarized below:

- A total of 161 nights in 2023, 157 nights in 2024, and 152 nights in 2025 exhibited detectable wave activity. Among these, waves with periods of 5–6 hrs were the most dominant and persistent, occurring on approximately 31% of the observed nights. This was followed by shorter-period waves in the 1–2 hrs range, which were identified on about 19% of the nights.

- Waves with periods shorter than 3 hrs are observed on 203 nights and exhibit largely irregular and non-periodic occurrence throughout the year. In contrast, waves with periods longer than 3 hrs are observed on 267 nights and exhibit a clear seasonal variability with a pronounced peak during the winter months (January–February and November–December) and trough during the summer months (April–September). This distinct periodic behaviour of long-period waves is quantitatively confirmed using Lomb–Scargle periodogram spectral analysis, which reveals a strong and consistent peak corresponding to an annual oscillation (365 days) across all three individual years of observation. On the other hand, shorter-period waves do not exhibit any statistically significant spectral peaks, and their distribution remains scattered and non-periodic.

514 — To investigate the role of background winds, the seasonal behaviour of long-period
515 waves is compared with the HWM14 derived horizontal wind components (U_x and U_y)
516 derived from the HWM14 model over the three year of observational period. A
517 quantitative assessment shows that the annual variation in wave periods has a stronger
518 statistical coherence with the U_y (R=0.78) than with U_x (R=0.68). Although both wind
519 components contribute to modulating wave propagation through filtering processes,
520 this difference indicates a comparatively greater influence of the meridional wind.
521 Notably, this occurs despite the U_x having a substantially larger magnitude (≈21 m/s),
522 nearly 2.7 times that of the U_y (≈8 m/s). This suggests that the directional characteristics
523 and interactions of waves with U_y are the primary controlling factors in the annual
524 modulation of long-period waves.

525 — The strong correlation coefficient of 0.89 between the long-period waves and U_h
526 indicating a strong positive relationship, demonstrating that their temporal variability
527 is closely coupled. This behaviour can be attributed to wind filtering, wherein
528 favourable background wind conditions prevent slow-moving, long-period waves from
529 encountering critical levels, thereby allowing them to propagate into the upper
530 atmosphere. As a result, the occurrence of long-period waves varies systematically with
531 U_h showing enhanced occurrence during winter months and reduced activity during
532 summer months in alignment with seasonal wind patterns.

533 — Short-period waves possess significantly higher c_h ($\gg U_h$), which allows them to
534 propagate efficiently through the background flow without being affected by wind
535 filtering. Consequently, their presence in the MLT region is largely independent of
536 seasonal variations in U_h. Instead, these waves are primarily governed by localized and
537 transient source mechanisms, such as convection or instabilities, and may even be

generated in situ within the MLT region rather than propagating upward from lower atmospheric layers.

In conclusion, the results identify a transition period near ~3 hrs that separates two distinct AGW regimes in the MLT region. Waves with periods longer than 3 hrs exhibit strong seasonal modulation that is closely linked to variations in the background horizontal wind field through selective wind filtering that permits or inhibits their propagation depending on their horizontal phase speed c_h. In contrast, waves with periods shorter than 3 hrs remain largely decoupled from wind-driven filtering processes and are instead governed by local and transient generation mechanisms rather than large-scale seasonal wind variations.

Declarations

Availability of data and materials

The datasets generated and/or analysed during the current study are available at https://www.prl.res.in/~ravindra/index_files/PAIRS_data_availability.zip. Additional PAIRS data can be provided on a request basis to Dr. Ravindra P Singh, PRL.

Competing interests

The authors declare that they have no competing interests.

Funding

This work was supported by the Department of Space, Government of India.

Authors' contributions

Kiran carried out the analysis and wrote the initial draft of the manuscript. RPS conceptualized, supervised, and edited the manuscript. RPS was responsible for the development and operation of the PAIRS. Both authors read and approved the final manuscript.

Author details

[a]Space and Atmospheric Sciences Division, Physical Research Laboratory, Navrangpura, Ahmedabad, 380009, India, [b]Indian Institute of Technology, Gandhinagar, 382355, India

Acknowledgments

This work at Physical Research Laboratory (PRL), Ahmedabad was supported by the Department of Space, Government of India. Kiran was working as SRF at Physical Research Laboratory during the period of this work. The PAIRS data utilized in this study were obtained from the Physical Research Laboratory (PRL), Ahmedabad.

References

Bretthorst, G. L. (1988). Bayesian spectrum analysis and parameter estimation. In Lecture notes in statistics. https://doi.org/10.1007/978-1-4684-9399-3.

Cao, B., & Liu, A. Z. (2022). Statistical characteristics of high-frequency gravity waves observed by an airglow imager at Andes Lidar Observatory. Earth and Space Science, 9, e2022EA002256. https://doi.org/10.1029/2022EA002256.

Deepa, V., Ramkumar, G., Antonita, M., Kumar, K. K., & Sasi, M. N. (2006). Vertical propagation characteristics and seasonal variability of tidal wind oscillations in the MLT region over Trivandrum (8.5° N, 77° E): first results from SKiYMET Meteor Radar. Annales Geophysicae, 24(11), 2877–2889. https://doi.org/10.5194/angeo-24-2877-2006.

Drob, D. P., Emmert, J. T., Meriwether, J. W., Makela, J. J., Doornbos, E., Conde, M., et al. (2015). An update to the horizontal wind model (HWM): The quiet time thermosphere. Earth and Space Science, 2, 301–319. https://doi.org/10.1002/2014EA000089.

Dunkerton, T. J. (1982). Theory of the mesopause semiannual oscillation. Journal of the Atmospheric Sciences, 39(12), 2681–2690. https://doi.org/10.1175/1520-0469(1982)039<2681:TOTMSO>2.0.CO;2.

585 Ejiri, M. K., Shiokawa, K., Ogawa, T., Igarashi, K., Nakamura, T., & Tsuda, T. (2003).
586 Statistical study of short-period gravity waves in OH and OI nightglow images at two
587 separated sites. Journal of Geophysical Research Atmospheres, 108(D21).
588 https://doi.org/10.1029/2002jd002795.

589 Fritts, D. C. and Alexander, M. J. (2003). AGWs Dynamics and Effects in the Middle
590 Atmosphere, Reviews of Geophysics, 41, 1003,
591 https://doi.org/10.1029/2001RG000106.

592 Garcia, R. R., and Solomon, S. (1985). The effect of breaking AGWs on the dynamics and
593 chemical composition of the mesosphere and lower thermosphere. Journal of
594 Geophysical Research: Atmospheres, 90(D2), 3850–3868.
595 https://doi.org/10.1029/jd090id02p03850.

596 Hecht, J. H., Walterscheid, R. L., Fritts, D. C., Isler, J. R., Senft, D. C., Gardner, C. S., &
597 Franke, S. J. (1997). Wave breaking signatures in OH airglow and sodium densities and
598 temperatures: 1. Airglow imaging, Na lidar, and MF radar observations. Journal of
599 Geophysical Research Atmospheres, 102(D6), 6655–6668.
600 https://doi.org/10.1029/96jd02619.

601 Hecht, J. H., Walterscheid, R. L., Hickey, M. P., & Franke, S. J. (2001). Climatology and
602 modeling of quasi-monochromatic atmospheric gravity waves observed over Urbana
603 Illinois. Journal of Geophysical Research Atmospheres, 106(D6), 5181–5195.
604 https://doi.org/10.1029/2000jd900722.

605 Hines, C. O. (1960). Internal atmospheric gravity waves at ionospheric heights. Canadian
606 Journal of Physics, 38(11), 1441–1481. https://doi.org/10.1139/p60-150.

607 Hocke, K., Kämpfer, N. (2009). Gap filling and noise reduction of unevenly sampled data
608 by means of the Lomb-Scargle periodogram. Atmospheric Chemistry and Physics,
609 9(12), 4197–4206. https://doi.org/10.5194/acp-9-4197-2009.

610 Hocke, K. (1998). Phase estimation with the Lomb-Scargle periodogram method. In Annales
611 Geophysicae-European Geophysical Society, 16, 356-358.

612 Kiran and R. P. Singh (2025a). Vertical wave characteristics in the MLT region and its seasonal
613 variations using OH(3-1) brightness and rotational temperature from Ahmedabad
614 (23ºN, 72.6ºE). Advances in Space Research. 75(7), 5484-5498,
615 https://doi.org/10.1016/j.asr.2025.01.017.

616 Kiran, & Singh, R. P. (2025b). On the latitudinal variations of AO, SAO, and ISOs in the MLT
617 temperatures. Advances in Space Research. https://doi.org/10.1016/j.asr.2025.10.003.

618 Krassovsky, V. I., Potapov, B. P., Semenov, A. I., Shagaev, M. V., Shefov, N. N., Sobolev, V.
619 G., & Toroshelidze, T. I. (1977). Internal gravity waves near the mesopause and the
620 hydroxyl emission. Annales de Geophysique, 33, 347-355.

621 Liu, A. Z., and Swenson, G. R. (2003). A modeling study of O_2 and OH airglow perturbations
622 induced by atmospheric AGWs. Journal of Geophysical Research: Atmospheres,
623 108(D4). https://doi.org/10.1029/2002jd002474.

624 Lomb, N. R. (1976). Least-squares frequency analysis of unequally spaced data. Astrophysics
625 and Space Science, 39(2), 447–462. https://doi.org/10.1007/bf00648343.

626 Lowe, R., LeBlanc, L., & Gilbert, K. (1996). WINDII/UARS observation of twilight behaviour
627 of the hydroxyl airglow, at mid-latitude equinox. Journal of Atmospheric and
628 Terrestrial Physics, 58(16), 1863–1869. https://doi.org/10.1016/0021-9169(95)00178-
629 6.

630 Reisin, E. R. and Scheer, J., (1996). Characteristics of atmospheric waves in the tidal period
631 range derived from zenith observations of O_2(0–1) Atmospheric and OH(6-2) airglow
632 at lower midlatitudes. Journal of Geophysical Research: Atmospheres, 101(D16),
633 21223-21232, https://doi.org/10.1029/96JD01723.

634 Scargle, J. D. (1982). Studies in astronomical time series analysis. II - Statistical aspects of
635 spectral analysis of unevenly spaced data. The Astrophysical Journal, 263, 835-853.
636 https://doi.org/10.1086/160554.

637 Sedlak, R., Zuhr, A., Schmidt, C., Wüst, S., Bittner, M., Didebulidze, G. G., & Price, C. (2020).
638 Intra-annual variations of spectrally resolved AGWs activity in the upper
639 mesosphere/lower thermosphere (UMLT) region. Atmospheric Measurement
640 Techniques, 13(9), 5117–5128. https://doi.org/10.5194/amt-13-5117-2020.

641 Shiokawa, K., Otsuka, Y., and Ogawa, T. (2009). Propagation characteristics of nighttime
642 mesospheric and thermospheric waves observed by optical mesosphere thermosphere
643 imagers at middle and low latitudes, Earth, Planets and Space, 61, 479–491,
644 https://doi.org/10.1186/BF03353165.

645 Singh, R. P., & Pallamraju, D. (2016). Effect of cyclone Nilofar on mesospheric wave
646 dynamics as inferred from optical nightglow observations from Mount Abu, India.
647 Journal of Geophysical Research Space Physics, 121(6), 5856–5867.
648 https://doi.org/10.1002/2016ja022412.

649 Singh, R. P. & Pallamraju, D., (2017). Large- and small-scale periodicities in the mesosphere
650 as obtained from variations in O_2 and OH nightglow emissions. Annales Geophysicae,
651 35, 227–237. https://doi.org/10.5194/angeo-35-227- 2017.

652 Singh, R. P., Pallamraju, D., Suryawanshi, P., Urmalia, S. (2023). Studies of atmospheric
653 waves by ground-based observations of OH(3-1) emission and rotational temperature

using PRL airglow InfraRed spectrograph (PAIRS). Journal of Atmospheric and Terrestrial Physics, 244, 106039. https://doi.org/10.1016/j.jastp.2023.106039.

Smith, A. K. (2012). Global Dynamics of the MLT. Surveys in Geophysics, 33(6), 1177–1230. https://doi.org/10.1007/s10712-012-9196-9.

Swenson, G. R., and Gardner, C. S. (1998). Analytical models for the responses of the mesospheric OH* and Na layers to atmospheric AGWs. Journal of Geophysical Research: Atmospheres, 103(D6), 6271–6294. https://doi.org/10.1029/97jd02985.

Tang, J., Liu, A. Z., and Swenson, G. R. (2002). High frequency AGWs observed in OH airglow at Starfire Optical Range NM: Seasonal variations in momentum flux, Geophysical Research Letters, 29, 27-1–27-4, https://doi.org/10.1029/2002GL015794.

Tarasick, D. W., & Hines, C. O. (1990). The observable effects of AGWs on airglow emissions. Planetary and Space Science, 38(9), 1105–1119. https://doi.org/10.1016/0032-0633(90)90019-m.

Taylor, M., & Hapgood, M. (1990). On the origin of ripple-type wave structure in the OH nightglow emission. Planetary and Space Science, 38(11), 1421–1430. https://doi.org/10.1016/0032-0633(90)90117-9.

Taylor, M. J., Ryan, E. H., Tuan, T. F., & Edwards, R. (1993). Evidence of preferential directions for gravity wave propagation due to wind filtering in the middle atmosphere. Journal of Geophysical Research Atmospheres, 98(A4), 6047–6057. https://doi.org/10.1029/92ja02604.

Taylor, M. J. (1997). A review of advances in imaging techniques for measuring short period gravity waves in the mesosphere and lower thermosphere, Advances in Space Research, 19, 667– 676.

Wüst, S., Bittner, M., Yee, J., Mlynczak, M. G., & Russell, J. M., III. (2020). Variability of the Brunt–Väisälä frequency at the OH*-airglow layer height at low and midlatitudes. Atmospheric Measurement Techniques, 13(11), 6067–6093. https://doi.org/10.5194/amt-13-6067-2020.

Wüst, S., Bittner, M., Espy, P. J., French, W. J. R., & Mulligan, F. J. (2023). Hydroxyl airglow observations for investigating atmospheric dynamics: results and challenges. Atmospheric Chemistry and Physics, 23(2), 1599–1618. https://doi.org/10.5194/acp-23-1599-2023.

Supplementary Files

This is a list of supplementary files associated with this preprint. Click to download.

- graphicalabstract.jpg